The Impact of Atmospheric Rivers on Precipitation and Their Contribution to Crustal Deformation in Greenland, 2010 to 2019

Wenhao Li, Xinyu Qin, Tingting Zhu, Jintao Lei, C. K. Shum, Fei Li, and Shengkai Zhang

***Abstract*—In recent years, the range and impact of atmospheric rivers (ARs) landing in Greenland have been increasing. Extreme precipitation brought by ARs can cause a short-term surge in regional ice and snow mass, resulting in "transient" signal in the coordinate time series of Greenland GNSS stations. However, previous studies have mainly focused on ARs detection and corresponding climate impact factors, lacking research on the contribution of extreme AR precipitation to crustal deformation. This article utilizes MERRA-2 reanalysis data and the vIVT algorithm to statistically analyze the frequency, duration, and spatiotemporal distribution of ARs landings in Greenland from 2010 to 2019. We quantitatively analyze the extreme precipitation events caused by ARs and their spatiotemporal evolution characteristics across Greenland and its basins. Then, using coordinates time series from 46 GNSS stations in Greenland, we extract the transient crustal deformation signals caused by AR-induced precipitation based on the multichannel singular spectrum analysis method. The results show that from 2010 to 2019, ARs landed in Greenland a total of 186 times, with a duration of 3174 h, and they showed an overall increasing trend. AR-induced precipitation in Greenland accounted for approximately 13.42% of annual precipitation, with the western region contributing more than 16%. Overall, the contribution rate of AR-induced rainfall was lower than that of AR-induced snowfall. Transient crustal deformation signals caused by AR-induced precipitation were found in some GNSS stations, with vertical deformation reaching up to 1 mm. Coastal areas showed greater deformation than inland areas, and low-latitude areas showed greater deformation than high-latitude areas.**

***Index Terms*—Atmospheric rivers (ARs), GNSS, precipitation, transient signals.**

Received 26 September 2024; revised 1 November 2024; accepted 8 December 2024. Date of publication 13 December 2024; date of current version 30 December 2024. This work was supported in part by the National Natural Science Foundation of China under Grant 42474042, in part by Guangxi Science and Technology Major Program under Grant AA23073017, in part by National Natural Science Foundation of China under Grant 42074006, in part by the Key Laboratory of Polar Environment Monitoring and Public Governance (Wuhan University), Ministry of Education under Grant 202304, in part by State Key Laboratory of Geo-Information Engineering under Grant SKLGIE2023-ZZ-1, and in part by The National Key Research and Development Program of China under Grant 2023YFC2809103. *(Corresponding authors: Tingting Zhu; Jintao Lei.)*

Wenhao Li is with the School of Geomatics Science and Technology, Nanjing Tech University, Nanjing 211816, China, and also with the State Key Laboratory of Geo-information Engineering, Xi'an 710054, China (e-mail: wh_li@whu.edu.cn).

Xinyu Qin and Tingting Zhu are with the School of Geomatics Science and Technology, Nanjing Tech University, Nanjing 211816, China (e-mail: qinxinyu@njtech.edu.cn; zhutingting62008@njtech.edu.cn).

Jintao Lei is with the School of Civil Engineering and Architecture, Guangxi University, Nanning 530004, China (e-mail: jintao.lei@gxu.edu.cn).

C. K. Shum is with the Division of Geodetic Science, School of Earth Sciences, The Ohio State University, Columbus, OH 43210 USA (e-mail: ck.shum@outlook.com).

Fei Li and Shengkai Zhang are with the Chinese Antarctic Center of Surveying and Mapping, Wuhan University, Wuhan 430079, China (e-mail: fli@whu.edu.cn; zskai@whu.edu.cn).

Digital Object Identifier 10.1109/JSTARS.2024.3517142

I. Introduction

ATMOSPHERIC rivers (ARs) are narrow corridors or filaments of concentrated water vapor in the atmosphere, characterized by enhanced water vapor transport [1]. ARs are an important component of the hydrological cycle, transporting water vapor from warm mid- and low-latitude regions to cold high-latitude regions, sometimes accompanied by intense precipitation (mainly snowfall and rainfall) [2], [3]. ARs can extend over great distances, even stretching from high sea-surface temperature areas in the subtropics to polar regions [4], [5]. In the warm sector of cyclones, warm and moist air is swept by advancing cold fronts, causing high moisture content filaments to be transported north and south at the base of the warm conveyor belt [6], [7], [8], [9], [10]. When topography lifts the landing moist air masses, it often triggers ARs to exhibit stable vertical stratification and produce heavy precipitation [3], [11], [12], [13], [14]. Under favorable atmospheric blocking conditions, as long as the moisture source continues to supply water vapor, a single AR event can persist for a long time [15], [16]. Mesoscale frontal waves can transmit successive vorticity maxima along the edge of the blocking ridge, causing ARs to sometimes consist of multiple rounds of heavy precipitation [6], [17], [18]. As ARs move toward the poles, they transport moisture to polar regions, leading to a short-term surge in polar precipitation, triggering extreme weather such as heavy rain, blizzards, and extreme cold [19], [20], [21], thereby increasing surface ice and snow mass and exacerbating crustal deformation [22], [23]. Overall, ARs impact polar environment and play an important role in global climate cycles [24], [25]. Since the 21st century, the Greenland Ice Sheet has shown an accelerating trend of mass loss [26], [27], [28], [29]. Studies on the mass balance of the Greenland Ice Sheet are typically described in terms of surface mass balance (SMB) processes and ice discharge at the grounding line, both of which are controlled by atmospheric and oceanic factors [30]. Mattingly et al. [31] found that summer AR landing events exacerbate surface melting of the Greenland Ice Sheet . Solid precipitation is the main input source for Greenland's SMB, and recent rapid melting events coincided with

intense moisture transport by ARs over Greenland, indicating that ARs have a significant impact on SMB changes [2], [25], [26], [32], [33], [34], [35], [36], [37], [38], [39], [40]. Mattingly et al. [65] discovered that ARs affecting northwestern Greenland triggered Foehn winds and subsequent intense melting events in northeastern Greenland. Neff et al. [43] found that AR events promote the melting of the Greenland Ice Sheet through the advection of air masses over the ocean, such as the two AR events in July 2012 that led to record-breaking ice sheet melting in Greenland [41], [42], [43] . In recent years, the frequency and number of AR landings in Greenland have been increasing. The abnormally high moisture content may lead to extreme precipitation events, which is a major source of mass gain for the Greenland Ice Sheet. Therefore, AR events directly affect the mass balance of Greenland's ice and snow [25], [44], [45], [46], [47], [48]. Although there has been extensive research on ARs, most studies have focused on AR detection and their impact on ice sheet SMB and climate change [25], [27], [37], [49], [50], [51], [52], [53], [54], [55], there is a lack of research that accurately quantifies and assesses the impact of AR on extreme precipitation events. In addition, the mass balance of the Greenland Ice Sheet is highly sensitive to short-term extreme weather events. Transient crustal deformation signals caused by heavy precipitation can enter GNSS coordinate time series, yet few scholars have conducted in-depth studies on this. Therefore, this article utilizes MERRA-2 reanalysis and GNSS coordinate time series to analyze the spatiotemporal evolution of AR landings in Greenland and its basins from 2010 to 2019. We also identify and separate the intense precipitation events triggered by ARs, along with the associated transient signals in crustal deformation detected by GNSS.

The rest of this article is organized as follows. Section II briefly introduces the data sources; Section III introduces the AR detection algorithm, the impact of AR on Greenland precipitation, and the algorithm to calculate crustal deformation caused by precipitation events. Section IV deeply analyzes the landing situations of AR in Greenland, their contribution to precipitation, and the resulting crustal displacement. Finally, Section V concludes this article.

II. Data

In this study, AR data come from the MERRA-2 vIVT hourly resolution data, spanning from January 1, 2010, to December 31, 2019, with a spatial resolution of 0.625°× 0.5°. For consistency, rainfall and snowfall data also come from MERRA-2, with the same spatial resolution of 0.625°× 0.5°and temporal resolution of 1 h. Currently, over 50 GNSS stations have been deployed around Greenland. After evaluating data quality and completeness, 46 stations were used in our study, covering the same time span from 2010 to 2019. Here, we adopt the convention proposed in [56] to divide Greenland into six basins: Northern (NO), Northeastern (NE), Southeastern (SE), Southwestern (SW), Central-Western (CW), and Northwestern (NW) regions. The locations of the GNSS stations used in the study and the regional divisions of Greenland are shown in Fig. 1. GNSS coordinate time series can be obtained from the Nevada Geodetic Laboratory with a temporal resolution of 5 min [57]. For the numerical calculation of Greenland's partitioning, we followed the criteria established in [58]. Their partitioning approach is more detailed and nuanced, dividing the region into smaller, well-defined areas, allowing for the independent analysis of these subregions. This detailed partitioning is particularly useful for conducting a more refined study of AR occurrences in Greenland. Data processing uses the final satellite orbit and clock products from the Jet Propulsion Laboratory (JPL) and is conducted using JPL's GipsyX software (version 1.0) in undifferenced and ionosphere-free modes. A priori troposphere information and related mapping functions come from VMF1 grids. Daily ionosphere products from JPL and IONEX data from the 12th generation International Geomagnetic Reference Field (IGRF12) are used to calibrate higher order ionospheric fluctuations. Other conventional geophysical and geodetic effects, such as solid Earth tides, ocean tidal loading, pole tides, phase center offsets and variations, relativistic effects, etc., have been corrected. The third quartile method is used to identify and eliminate gross errors in the GNSS coordinate time series.

III. Methodology

A. AR Detection Algorithm

ARs transport water vapor from mid- and low-latitude regions to high-latitude regions, where they generate intense precipitation events. To quantify AR's contribution to precipitation in Greenland, this article uses the AR category obtained from the Climate Data at the NSF National Center for Atmospheric Research based on the vIVT (an updated version of the meridional (v) component of integrated vapor transport) algorithm. The vIVT is an enhancement of the original IVT detection algorithm, with the addition of the meridional (v) component. By identifying grid cells between 59.5°N and 84°N, we obtained monthly vIVT values for Greenland from 2010 to 2019 and filtered out values where vIVT is less than the 98th percentile. If an air mass has a vIVT value greater than the 98th percentile and the filament of the air mass extends at least 20° in the meridional direction, it is identified as an AR event. The calculation method for vIVT is as follows:

$$\text{vIVT} = -\frac{1}{g}\int_{\text{surface}}^{\text{top}} q v_m dp \tag{1}$$

where $\text{g}(\text{ms}^{-2})$ is the gravitational acceleration, $q(\text{kgkg}^{-1})$ is the specific humidity at a given atmospheric pressure level, and dp is the pressure level. The vIVT updates the consideration of the meridional wind speed component $v_m(\text{ms}^{-1})$ based on IVT.

The IWV, IVT, and vIVT algorithms are all designed for water vapor detection, with the key difference being that ongoing research has shown the use of different algorithms in polar regions can enhance the accuracy and completeness of AR detection. All three methods integrate specific humidity under certain atmospheric pressures. In our earlier work, the IWV method was employed, but it was later upgraded to IVT for improved detection accuracy. In fact, the vIVT used in this study is an enhanced version of the IVT algorithm, which further incorporates radial wind velocity [25], [37], [51]. This addition

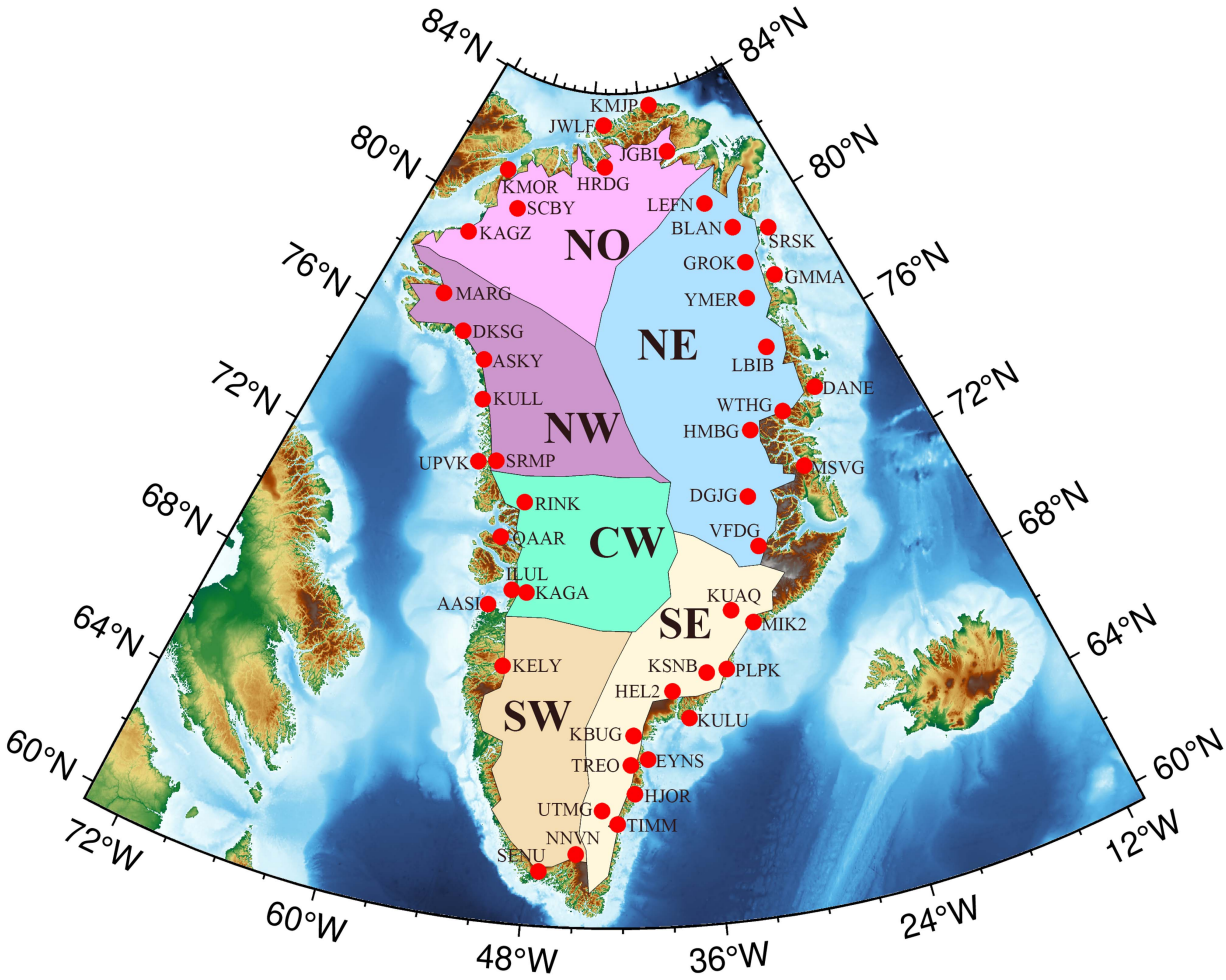

Fig. 1. Distribution of GNSS station locations and the division of the Greenland Island.

proves more advantageous for the detection and identification of ARs.

To obtain the detailed evolution process of AR landing and leaving Greenland, this article establishes an AR detection category. First, AR detection is performed using vIVT to obtain the time points and duration of AR occurrences. By analyzing the spatial range of AR during each time span, the spatiotemporal data of each AR event are obtained. All AR events from 2010 to 2019 are uniformly detected and processed, excluding those AR events that did not land within the mainland of Greenland, resulting in the final AR detection category. The specific technical route is shown in Fig. 2.

To identify areas with frequent AR occurrences, we process AR data as follows: when an AR reaches Greenland, grid cells within its spatial range are set to 1, indicating an AR event, while cells outside are set to 0. By analyzing all AR data, we generate a normalized matrix for each event. Summing these annually gives the number of AR events per location. The specific method is shown in Fig. 3. By aggregating these values over 2010–2019, we obtain the total AR occurrences at each location for the decade.

The spatial matrix used in this study supports the contribution calculation module by translating actual geographic locations into a matrix format for easier computation. The aim is to input data, such as snowfall, into the matrix and analyze contributions through matrix operations. This model is particularly useful for implementing normalization calculations, which will enhance the accuracy of frequency statistics.

B. AR Precipitation Contribution

To accurately calculate the precipitation contribution of AR, the data of rainfall, snowfall, and AR events are all converted into 3-D spatiotemporal matrices. During this process, it is ensured that the positions in the 3-D spatiotemporal matrices of the three variables correspond exactly, thus unifying the actual positions of the relevant variables with their positions in the matrices. This ensures the normal computation of subsequent data at the corresponding spatial locations. The spatial resolution of the AR and precipitation data used in this study is $0.625^\circ \times 0.5^\circ$. Based on this spatial resolution, corresponding spatial matrices for the three variables are created, where columns represent longitude, rows represent latitude, and the matrix size is $50\times$ 99. The matrix is shown as (2), where t represents time; such 2-D spatial matrices are overlaid to form a spatiotemporal matrix . Similarly, slicing the 3-D spatiotemporal matrix by time yields spatial

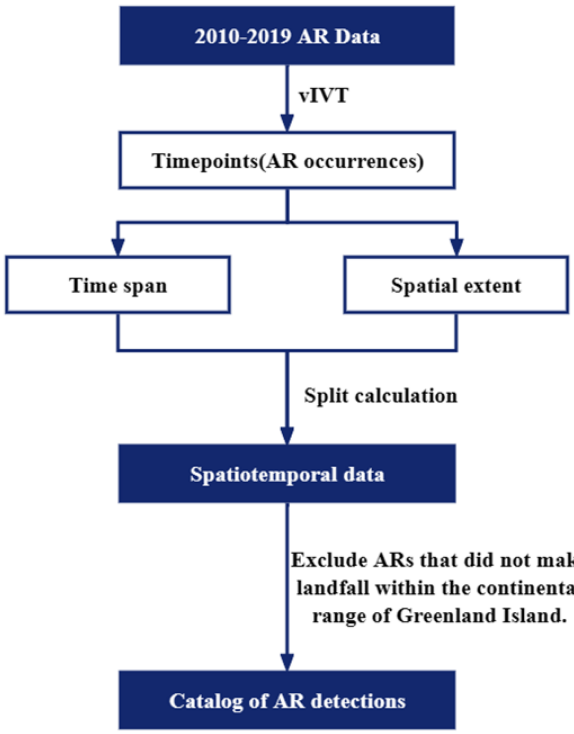

Fig. 2. Flowchart of the AR detection algorithm.

matrices. The conversion method for the matrices is shown in (3) and (4).

$$\begin{bmatrix} 1 & \cdots & m \\ \vdots & \ddots & \vdots \\ n & \cdots & n*m \end{bmatrix} \tag{2}$$

$$\text{Col} = \left(\frac{J + 59.5}{R_1}\right) + 1 \tag{3}$$

$$\text{Row} = \left(\frac{W + 11.875}{R_2}\right) + 1 \tag{4}$$

with $n = 50$ and $m = 99$. In (3) and (4), J and W represent the longitude and latitude boundaries of the AR, respectively. $R_1 = 0.625$ and $R_2 = 0.5$ indicate spatial resolution. Col refers to the columns of the transformed matrix; Row refers to the rows of the transformed matrix; and 59.5 and 11.875 correspond to the minimum boundaries of longitude and latitude, respectively.

AR precipitation refers to rainfall and snowfall events caused by ARs. We define AR-related precipitation as the rainfall and snowfall that falls within the footprint of the AR events. Research shows that 24 h after an AR event, the average cumulative precipitation decreases by more than 80% [59], and thereafter, the precipitation rate declines more slowly and levels off. To better demonstrate the impact of AR on precipitation, this study defines AR precipitation as the total precipitation during an AR event and within the following 24 h, thereby enabling a more accurate identification of rainfall and snowfall induced by AR.

First, we conduct a statistical analysis of the AR detection category to determine the time points and durations of AR occurrences. Second, we generate spatial matrices for rainfall and snowfall based on the spatial resolution of the AR data (corresponding to the latitudes and longitudes where the AR occurs). Finally, we align hourly rainfall and snowfall data with the AR detection category and create corresponding 3-D spatial matrices for precipitation from different AR events. By summing these matrices, we can obtain the total magnitude of rainfall and snowfall for each AR event. In addition, by aggregating rainfall and snowfall caused by all AR events within a given year, we can further quantify the spatial distribution of AR-induced precipitation for that year.

By summing the AR rainfall and snowfall for all locations in a given year, the total AR rainfall and snowfall for that year can be obtained. To determine the ratio of AR rainfall and snowfall to the annual total rainfall and snowfall, it is also necessary to calculate the total annual rainfall and snowfall. Similarly, by summing the spatial matrices of all rainfall and snowfall within the study area for that year, the spatial distribution of the total annual rainfall and snowfall can be obtained. In addition, by further merging the obtained rainfall and snowfall data, the total annual precipitation can be derived. According to the following formulas, the corresponding contribution rates of AR rainfall and snowfall can be obtained:

$$P_S = \frac{\text{ArS}}{\text{TotS}} \tag{5}$$

$$P_R = \frac{\text{ArR}}{\text{TotR}} \tag{6}$$

where P_S represents the AR snowfall contribution ratio, P_R represents the AR rainfall contribution ratio. ArS and ArR represent AR snowfall and rainfall, respectively, and TotS and TotR represent the annual total snowfall and rainfall, respectively. This formula can be used to calculate the contribution ratios from 2010 to 2019, and further calculate the total contribution rates of rainfall and snowfall over the ten years.

The impacts of AR events are typically short-term and intense, categorizing them as extreme events. Therefore, during AR occurrences, the observable or calculated data differ significantly compared to non-AR periods. During this time, the extreme characteristics of ARs often manifest as heavy precipitation or rainfall. Thus, once the precise timing and duration of AR landfalls are determined, our focus shifts to analyzing the data during these periods, particularly assessing the contribution to snowfall.

C. Impact of AR Precipitation on Crustal Deformation

To further quantify the crustal deformation induced by extreme AR precipitation, this study uses the load deformation calculation software LoadDef [60] to convolve the precipitation (rainfall and snowfall) mass from the MERRA-2 reanalysis data. This allows for the calculation of the relative displacement of crustal load deformation caused by precipitation at 46 GNSS stations between 2010 and 2019. To study the displacement effects caused by AR-induced rainfall and snowfall over a continuous ten-year period, we first merges all rainfall data from 2010 to 2019 into a complete dataset arranged in a time series (the same method is applied to snowfall data). Using the time of

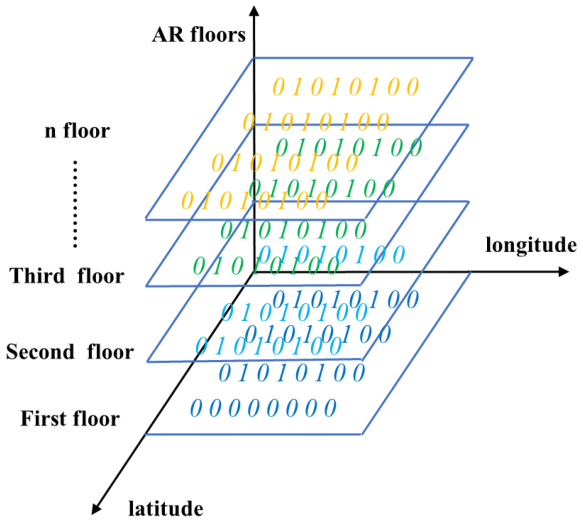

Fig. 3. Normalized superposition of AR landfalls.

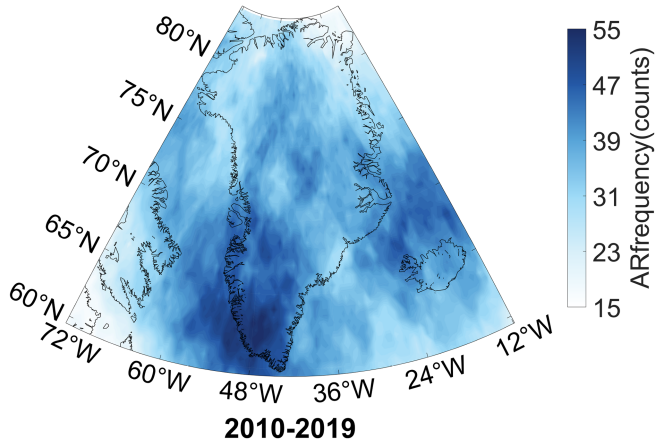

Fig. 4. Frequency and distribution of AR landfalls in Greenland from 2010 to 2019.

AR events landing in Greenland as the starting point and 24 h after leaving Greenland as the endpoint, the precipitation amount for each AR event is calculated. By extending the duration of AR events, errors in identifying AR time points and calculating AR precipitation amounts are prevented, thus avoiding any impact on subsequent results. Finally, the displacement caused by AR-induced rainfall and snowfall in Greenland is calculated to obtain 3-D surface displacements. This study uses the singular spectrum analysis (SSA) method to extract and analyze the crustal deformation signals induced by AR. SSA utilizes both the spatial and temporal correlations of geophysical fields to detect various signals without requiring prior information from stochastic models, making it flexible for application to various types of data. Based on these advantages, we chose SSA to detect and study the transient changes in glacier mass.

SSA has extraordinary ability to handle nonlinear time-series data, and the original time series can be decomposed into multiple signal components, each of which can be categorized into a periodic component, a quasi-periodic component, a noise component, and a trend component. It has been widely used in GNSS coordinate time-series analysis [51], [61], [62], [63]. Regarding the setting of the window, we generally rely on a rule of thumb to test the window near one-third of the total time series length.

IV. Results and Discussion

A. Analysis of AR Landfall

We analyzed the frequency and range of AR landfalls in Greenland from 2010 to 2019 (see Fig. 4) and tabulated the number and duration of AR landfalls by basin in Table I. The results show that AR made a total of 186 landfalls in Greenland over the past decade, with a cumulative duration of 3 174 h. Landfalls were more frequent in the SW and SE regions, with 56 and 54 occurrences, respectively, lasting for 1 287 and 1 191 h, respectively. Landfalls were less frequent in the NO, NW, and NE regions, with only 41 occurrences and 468 h in the NO region.

TABLE I
Frequency and Total Duration of AR Landings in Each Basin

Region	Counts	Hours
NW	44	554
NO	41	468
CW	51	932
NE	46	717
SW	55	1287
SE	53	1191

Fig. 5 presents the annual statistics on the number and range of AR landfalls. Most AR events follow a relatively narrow north-south trajectory along the eastern or western coastline. AR landfalls are more frequent near the southwestern coastline of Greenland, not only penetrating extensively into inland areas but also gradually extending northward along the coastline. On the eastern side, AR events are mostly concentrated near the coastline, with some events in 2016 and 2019 almost crossing the entire Greenland.

B. Analysis of AR Rainfall and Snowfall

Fig. 6 shows the number and durations of AR landfalls in Greenland and the rainfall and snowfall caused by AR, as well as their contributions to the total rainfall and snowfall. Fig. 6(a) shows the correlation between the number of AR landfalls and their duration. Fig. 6(b) illustrates the contribution rates of AR to rainfall and snowfall, while Fig. 6(c) and (d) shows the relationship between contribution rates and time for AR snowfall and AR rainfall, respectively. Fig. 6(e) and (f) displays the AR snowfall and rainfall amounts and their contribution rates. The average contribution of AR to rainfall and snowfall in Greenland is about 13.42%. Except for the years 2011, 2012, and 2017, the contribution rate of snowfall is generally higher than that of rainfall. Fig. 6(a) shows AR duration (left blue axis) and the number of landfalls (right red axis), indicating a clear correlation between the two variables. In 2011 and 2014, the number and duration of AR landfalls in Greenland were at their lowest during the study period. After 2014, the number of AR landfalls showed a slow upward trend. From 2010 to 2019, the number of AR

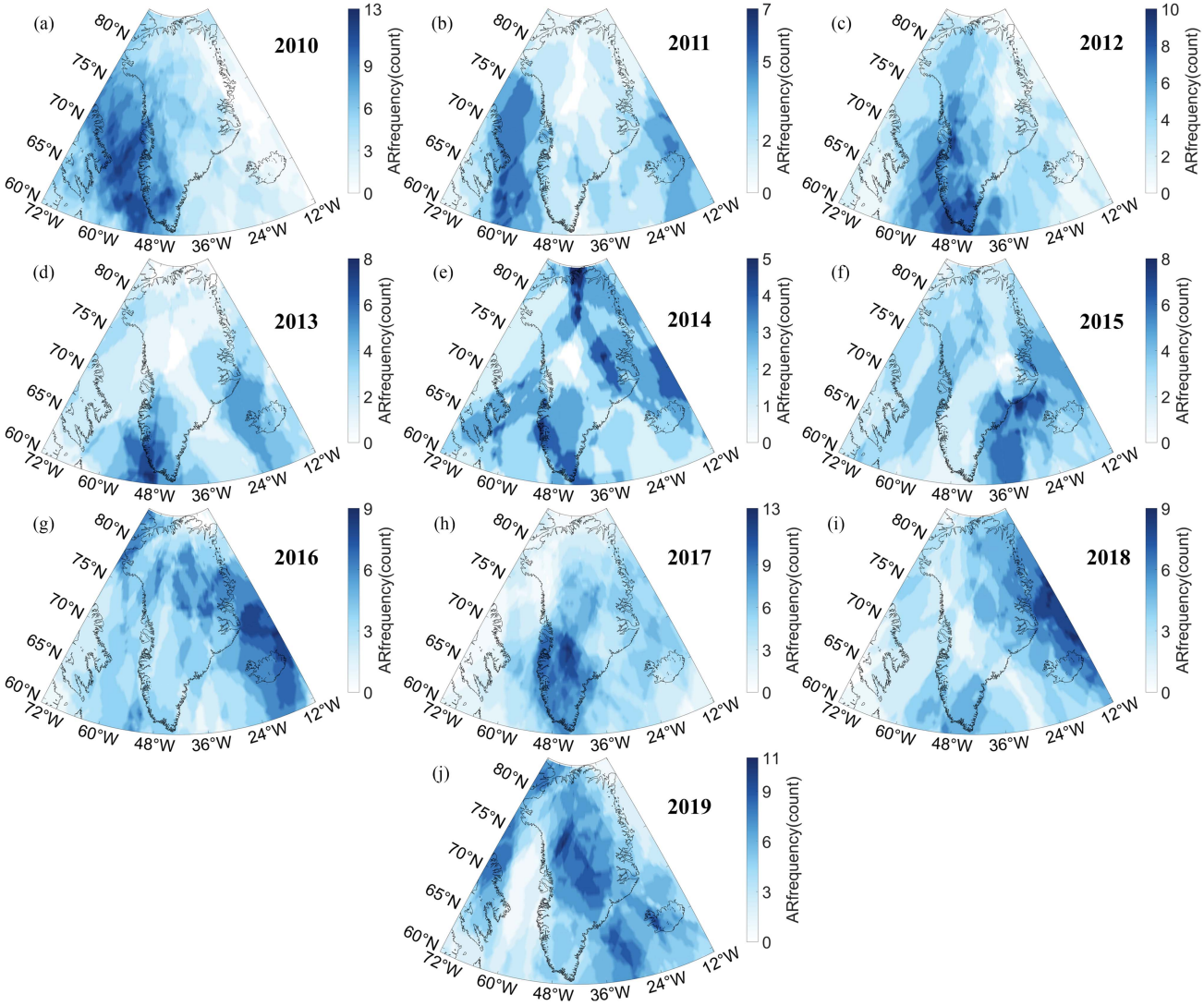

Fig. 5. Frequency and range of AR landfalls from 2010 to 2019. (a)-(j) shows the frequency and range of AR landfalls from 2010 to 2019.

landfalls ranged from 14 to 27, with durations between 156 and 465 h. The peak year was 2010 (27 times, 465 h), and the lowest was in 2014 (14 times, 156 h), with a sharp decline in 2011 (15 times, 189 h). Overall, since 2014, both the number of landfalls and their duration have shown a slow growth trend. In 2018, although the landfall duration did not significantly decrease (375 h in 2018 versus 386 h in 2017), the number of landfalls decreased (17 times in 2018 versus 21 times in 2017). Analysis shows that the average duration of each AR landfall that year was slightly higher than the ten-year average, with one extreme AR event lasting up to 60 h. Fig. 6(c) and (d) demonstrates the correlation between AR landfall duration and AR contribution. The significant positive relationship between the two suggests that the longer the AR landfall duration, the greater its contribution to rainfall and snowfall. In 2017, there was an abnormal increase in rainfall contribution despite no increase in AR landfall duration. This was due to multiple extreme rainfall events that year [15]. Fig. 6(e) and (f) quantifies AR rainfall and snowfall amounts and indicate their respective contribution rates. Fig. 6(c) and (d) shows the relationship between rainfall contribution and snowfall contribution, revealing that except for the years 2010, 2012, and 2017, the trend lines of their contribution rates generally match. It is noteworthy that 2010 and 2012 were relatively warm years; as AR duration increased, temperatures also rose, leading to a higher rainfall contribution rate.

Fig. 7 shows the snowfall and rainfall caused by AR from 2010 to 2019, as well as the total snowfall and rainfall in Greenland. Rainfall and snowfall are mostly concentrated along the southeastern coast of Greenland, with cumulative snowfall reaching up to 29 565.4 mm and cumulative rainfall totaling 18 906.6 mm. In the coastal areas of SW and SE, AR rainfall is relatively high, reaching up to 1 706.97 mm, while it is lowest in the NO and NE regions. AR snowfall is most prevalent in the southernmost part of SW, reaching up to 3 081.24 mm, and is distributed north-south along the SE coast, with the NO region having the least AR snowfall. To study the contribution rates of AR-induced rainfall and snowfall in different regions of Greenland, we divided Greenland into six regions: SE, SW, NE, NW, NO, and CW for analysis. Fig. 8 visualizes the AR contribution rates in

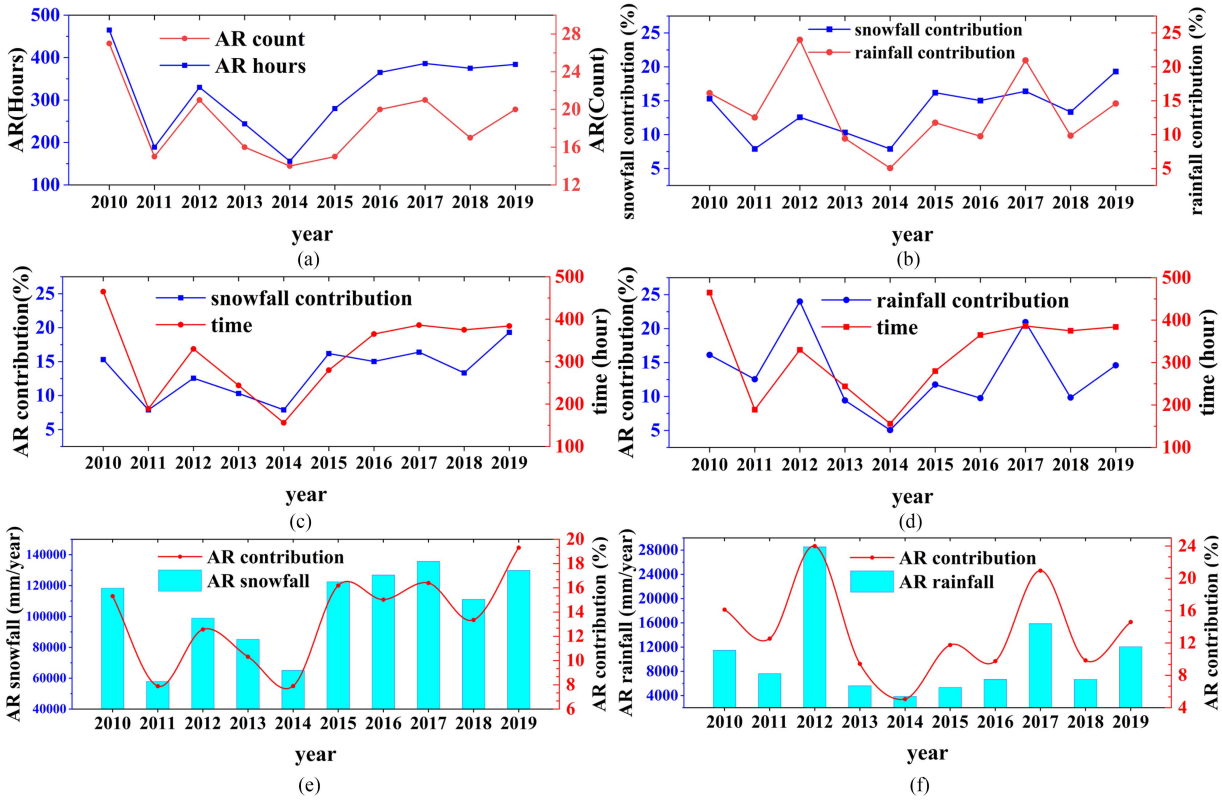

Fig. 6. Correlation analysis of the AR contribution. (a) shows the relationship between the number of AR login times and the duration; (b) shows the relationship between rainfall contribution and snowfall contribution. (c) and (d) show the relationship between rainfall contribution and time, and the relationship between snowfall contribution and time respectively. (e) and (f) respectively show the relationship between AR snowfall contribution rate and AR snowfall, and the relationship between AR rainfall contribution rate and AR rainfall.

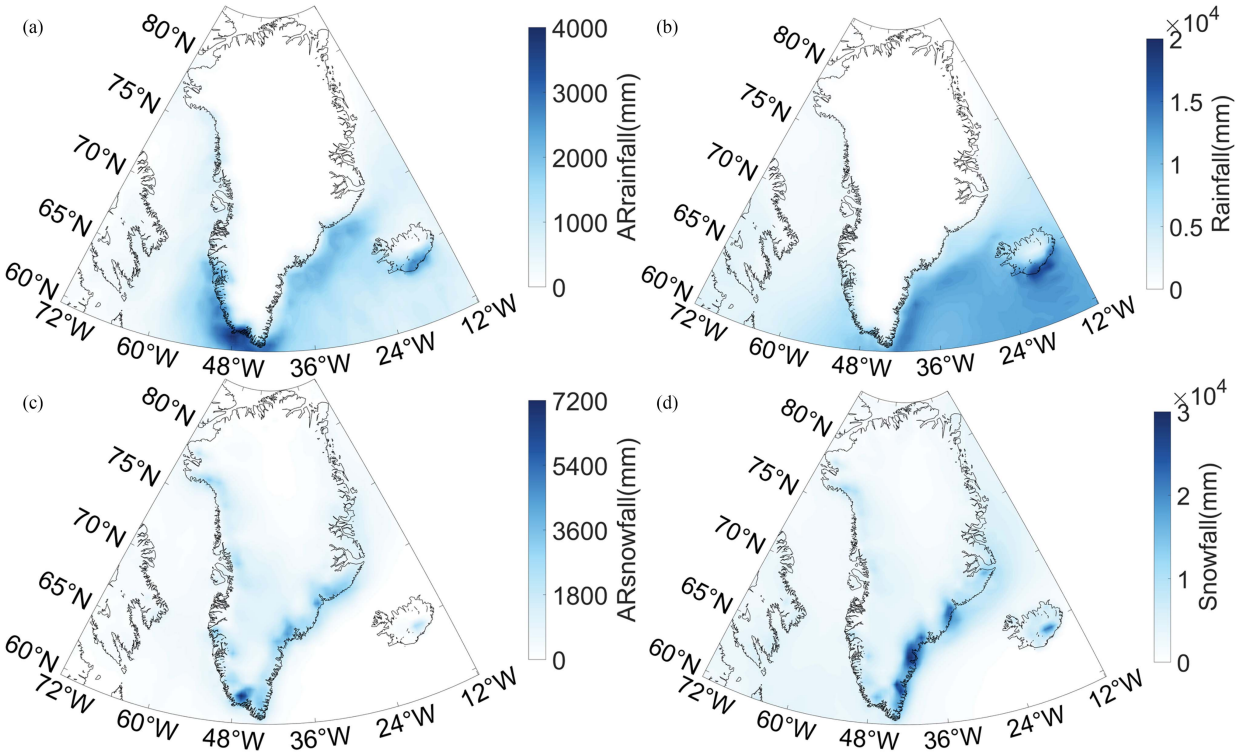

Fig. 7. AR rainfall, AR snowfall, total rainfall, and total snowfall from 2010 to 2019. (a) presents the AR rainfall from 2010 to 2019, (b) illustrates the total rainfall during the same period, (c) depicts the AR snowfall from 2010 to 2019, and (d) demonstrates the total snowfall over this timeframe.

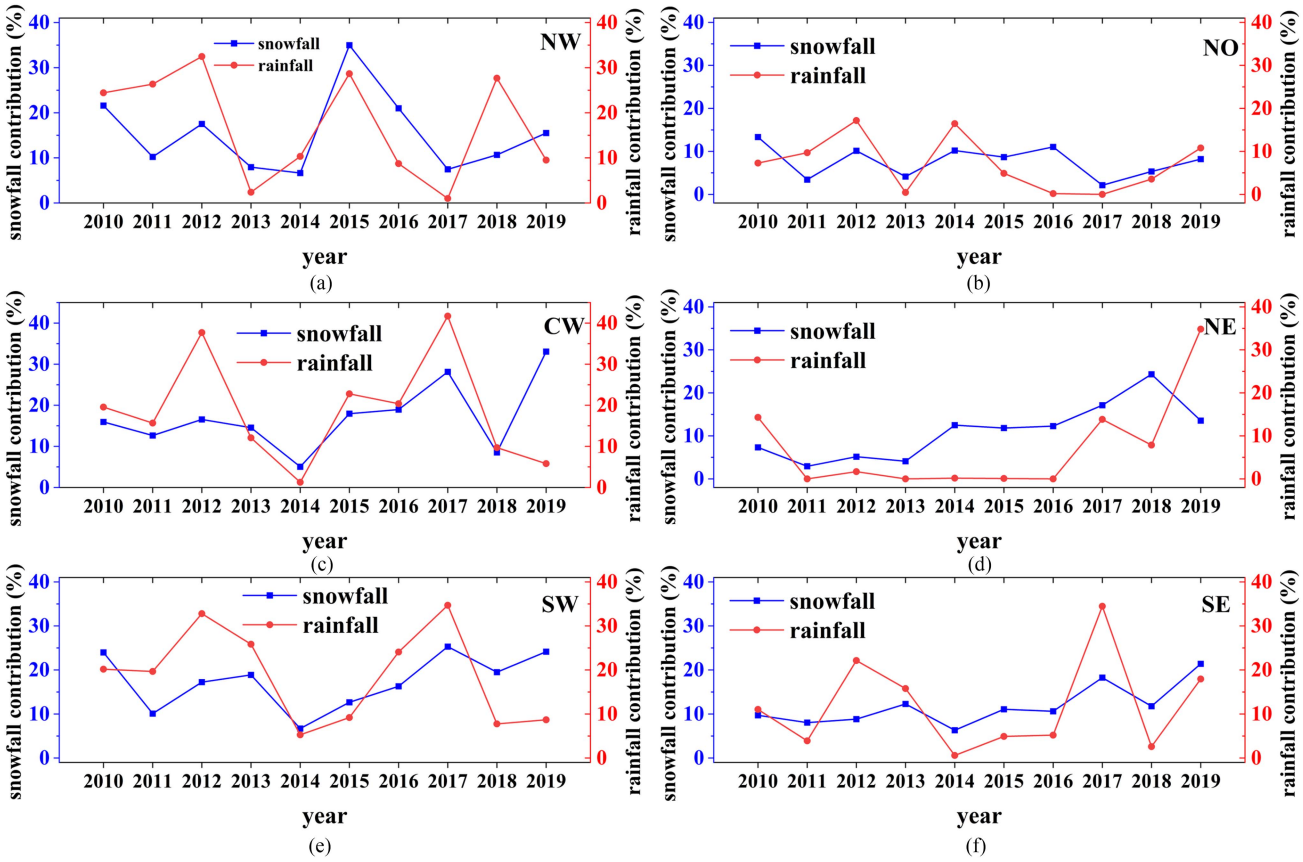

Fig. 8. Regional analysis of the contribution rate of AR-induced precipitation. (a) to (f) present the relationship between the contributions of AR-induced rainfall and snowfall across different regions.

different regions over ten years. The average AR contribution rates in the SW, CW, and NW regions of Greenland are all above 16%, with the SE region at 11.84%, while the NE and NO regions are lower, at only 7.35% and 9.19%, respectively. Overall, the AR contribution to Greenland's rainfall and snowfall from 2010 to 2019 generally ranges from 5% to 24% for rainfall and 8% to 20% for snowfall. Considering the impact of AR on rainfall and snowfall, it is found that the SW region is a key area for AR-induced rainfall and snowfall. This indicates that AR has a significant impact on the southern part of Greenland, especially near the SW region. According to the data in Fig. 8, it is evident that the contribution of AR to rainfall and snowfall is mainly concentrated in the western coastal region and the southern region of Greenland. It is speculated that this is because most ARs have a north–south orientation, transporting water vapor from south to north, resulting in the highest contribution rate in the SW region. In addition, as ARs move northward, the contribution rates in SW, CW, and NW regions decrease sequentially. Based on AR landfall data, the SE region has fewer AR landfalls compared to the western coastal areas, leading to a relatively lower contribution rate. Due to these two factors, and because the NE and NO regions are mostly inland with the SE region intercepting most AR precipitation near the coastline, the AR contribution rates in NE and NO regions are lower. Only in a few years when ARs frequently cross Greenland do these regions see a noticeable increase in AR contribution rates.

C. Identification and Separation of AR-Induced Transient Signals

The intense precipitation caused by AR can further affect crustal deformation in the Greenland region. We used LoadDef to calculate the crustal deformation displacement caused by AR precipitation, with some results shown in Fig. 9. Fig. 9(a) and (b) displays the relative displacement at the SENU station caused by snowfall from 2010 to 2019 and for the year 2010, respectively. Fig. 9(c) and (d) shows the relative displacement at the SENU station caused by rainfall. The vertical displacement caused by rainfall and snowfall is greater than the horizontal displacement, reaching over 1.5 mm, with the maximum displacement caused by rainfall at the SENU station even reaching up to 2.84 mm. Combining the AR occurrence times extracted in Section IV-A for the year 2010, several longer duration events were marked in the figures. There is a significant seasonal difference between the peak displacement fluctuations caused by rainfall and those caused by snowfall. The peak displacement fluctuations due to rainfall are mostly concentrated in summer, while those due to snowfall are mostly concentrated in winter. Table II summarizes the GNSS displacement caused by AR over ten years. The first column of the table indicates the region of Greenland where the station is located, the second column shows the station name, the third and fifth columns show the maximum displacement values caused by snowfall and rainfall, respectively, and the fourth and sixth columns show the average annual displacement

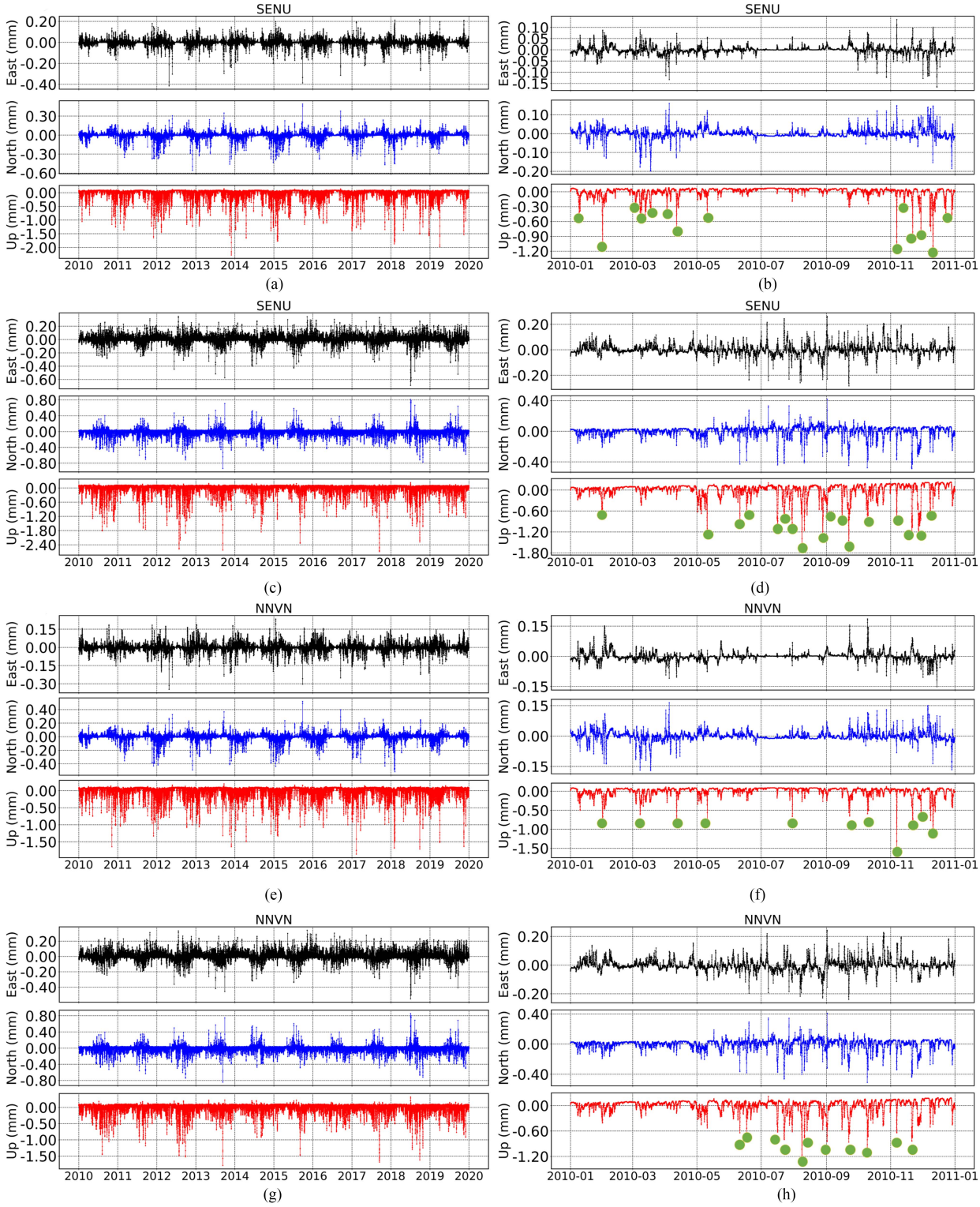

Fig. 9. Displacement for AR snowfall and rainfall. The left column represents the displacement over the past decade, while the right column represents the displacement for the year 2010. (a) and (c) illustrate the displacement at the SENU station caused by AR-induced rainfall and snowfall from 2010 to 2019, while (b) and (d) depict the displacement caused by AR-induced rainfall and snowfall at the same station in 2010. (e) and (g) illustrate the displacement at the NNVN station caused by AR-induced rainfall and snowfall from 2010 to 2019, while (f) and (h) depict the displacement caused by AR-induced rainfall and snowfall at the same station in 2010.

TABLE II
GNSS STATION DISPLACEMENT CAUSED BY ARS (MILLIMETER)

region	GNSS	Max-snow	Avg- snow	Max-rain	Avg- rain	Dist(km)
SE	TREO	2.64	0.14	2.85	0.06	0.09
	KULU	2.37	0.11	2.84	0.06	0.14
	HJOR	2.23	0.12	2.89	0.06	0.40
	LYNS	2.41	0.14	3.09	0.06	0.53
	PLPK	2.32	0.12	1.82	0.05	0.69
	MIK2	2.36	0.11	1.32	0.04	0.95
	TIMM	2.10	0.12	3.86	0.06	1.19
	KBUG	2.43	0.14	3.59	0.05	1.47
	HEL2	1.89	0.11	2.40	0.05	5.19
	KUAQ	1.77	0.10	1.24	0.04	11.34
	UTMG	1.92	0.12	3.38	0.06	21.00
	KSNB	1.85	0.11	1.68	0.05	48.18
SW	KELY	1.12	0.07	1.79	0.05	2.00
	SENU	2.37	0.10	2.87	0.06	11.81
	NNVN	1.97	0.11	1.73	0.06	51.48
CW	QAAR	1.13	0.07	2.32	0.05	0.15
	AASI	1.34	0.06	2.18	0.05	0.37
	ILUL	1.27	0.06	2.18	0.04	0.52
	KAGA	1.24	0.07	1.79	0.04	7.08
	RINK	0.99	0.07	1.67	0.03	27.19
NW	UPVK	0.93	0.06	1.96	0.03	0.22
	KULL	0.82	0.06	1.31	0.03	0.27
	ASKY	0.98	0.07	1.25	0.03	3.35
	SRMP	0.90	0.06	1.88	0.03	8.85
	MARG	1.04	0.06	1.75	0.03	9.90
	DKSG	1.17	0.07	1.75	0.03	14.88
NO	KMOR	0.72	0.04	1.20	0.02	1.22
	KAGZ	0.92	0.05	1.16	0.02	2.61
	KMJP	1.38	0.05	1.36	0.02	2.94
	JWLF	1.10	0.05	1.32	0.02	4.38
	JGBL	0.79	0.05	1.25	0.02	8.53
	HRDG	0.98	0.05	1.22	0.02	9.52
	SCBY	0.70	0.05	1.10	0.02	82.32
NE	GMMA	1.56	0.06	1.56	0.03	0.82
	DANE	1.47	0.07	1.82	0.03	0.88
	MSVG	1.49	0.08	2.06	0.03	1.08
	NRSK	1.34	0.06	1.10	0.03	2.54
	WTHG	1.24	0.07	1.30	0.03	17.33
	VFDG	1.20	0.08	1.84	0.04	25.00
	LEFN	0.87	0.05	1.10	0.02	29.37
	HMBG	1.00	0.06	1.38	0.03	32.47
	DGJG	1.02	0.07	1.83	0.03	50.42
	LBIB	1.08	0.06	1.40	0.03	53.04
	BLAS	1.24	0.05	1.02	0.02	56.68
	YMER	1.29	0.06	1.20	0.03	63.05

of GNSS stations considering the effects of snowfall and rainfall, respectively. The seventh column indicates the distance from the GNSS station to the coastline. To determine the impact of distance from the coastline on displacement, both maximum displacement and average displacement were analyzed. The results indicate that AR-induced snowfall can cause a maximum GNSS station displacement of up to 2.64 mm, while AR-induced rainfall can cause a maximum displacement of up to 3.86 mm. Overall, rainfall causes a higher maximum displacement than snowfall, whereas the average displacement due to rainfall is less than that due to snowfall. Generally, at similar latitudes, stations closer to the coastline experience greater displacement; latitude is also a significant factor affecting displacement. In the SW, SE, CW, and NW regions, stations located further south experience greater displacement. Considering both snowfall and rainfall impacts, stations affected by snowfall show significantly greater average displacement compared to those affected by rainfall. This suggests that snowfall has a more substantial impact on station displacement compared to rainfall. The greater maximum displacement caused by rainfall compared to snowfall is believed to be due to extreme weather events in warmer years .

SSA can decompose and reconstruct time series to handle nonlinear time series data. By decomposing the raw GNSS coordinate time series into a series of signal components, each

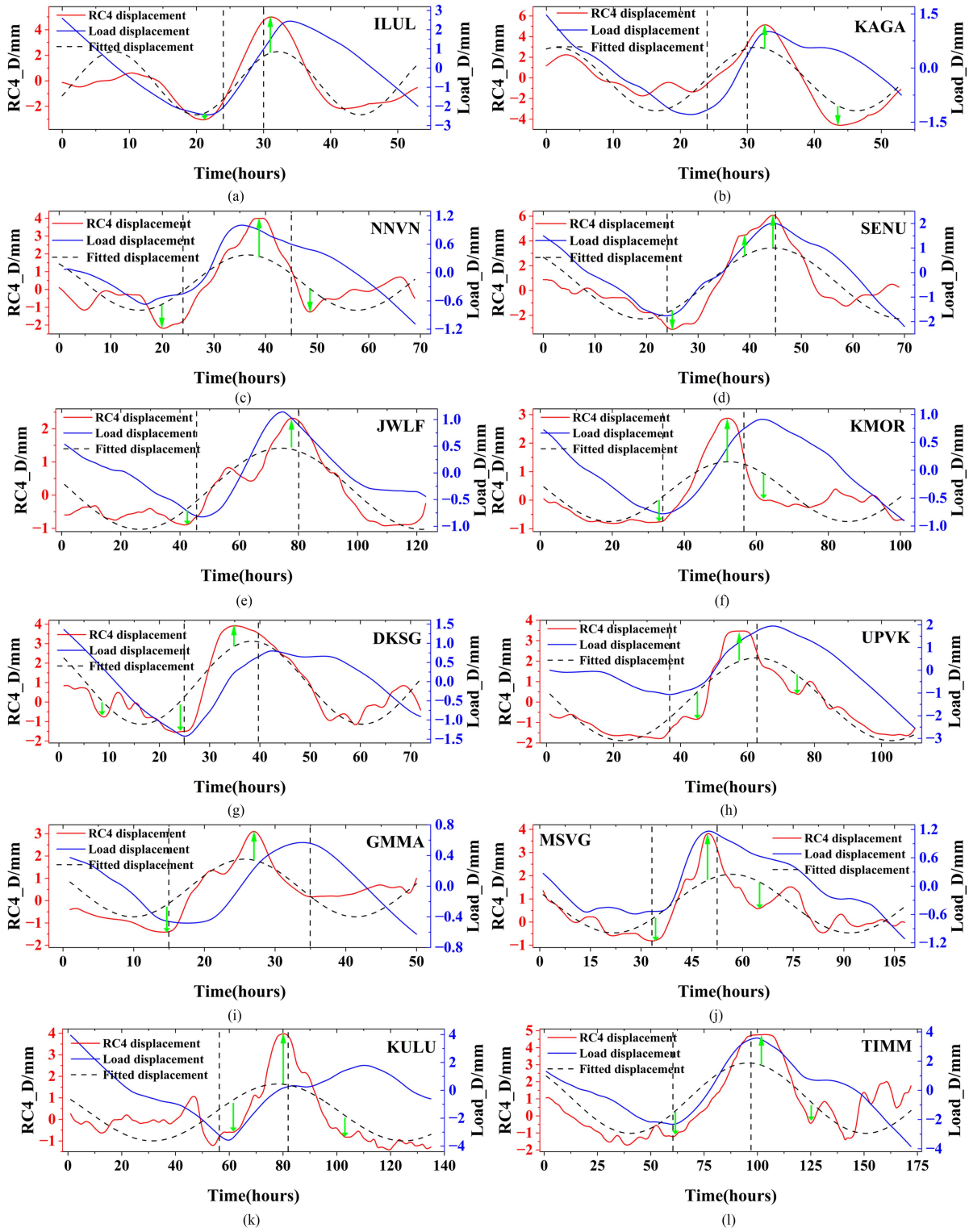

Fig. 10. Verification of displacement signals and deformation contributions caused by ARs. (a) to (l) validate the displacement signals and deformation contributions caused by ARs at different stations.

component can be divided into periodic, quasi-periodic, noise, and trend components. SSA analysis was performed on GNSS stations to verify AR signals, and the deformation contribution analysis is summarized in Fig. 10.

For Fig. 10(a) and (b), the data length is 635 h with a window setting of 54 h; for Fig. 10(c) and (d), the data length is 875 h with a window setting of 71 h. Fig. 10(a)–(d) represent the signal analysis for the ILUL and KAGA stations in the CW region and the NNVN and SENU stations in the SW region during a certain AR landfall period; Fig. 10(e) and (f) represent the JWLF and KMOR stations in the NO region; Fig. 10(g) and (h) represent the DKSG and UPVK stations in the NW region; Fig. 10(i)

and (j) represent the GMMA and MSVG stations in the NE region; Fig. 10(k) and (l) represent the KULU and TIMM stations in the SE region. The red curve indicates the AR displacement component signal extracted from GNSS, while the black curve represents the GNSS-AR fitted displacement signal, which is a simulated curve close to the theoretical value mainly used for comparing AR-induced signal changes. The blue curve shows the displacement component signal caused by AR-induced precipitation. By combining the rainfall and snowfall displacement components for the same period, the displacement component of precipitation can be obtained.

The black vertical lines indicate the time of AR occurrence. Based on the results of the three curves in Fig. 10, combined with the AR duration, we analyze the correlation between GNSS-derived AR-related displacement and AR precipitation displacement. The displacement amplitude of GNSS stations significantly increases during AR occurrences. The peak GNSS displacement lags slightly behind AR events. As shown in the GNSS stations SENU and NNVN, load deformation does not reach its peak during AR events but shows a continuous increasing trend, and finally, peaks after the AR ends. Considering that precipitation is a continuous accumulation process—the longer the time, the more precipitation accumulates—it can be concluded that crustal deformation displacement caused by AR aligns well with signals extracted from GNSS. The KULU station in the SE region shows an AR-induced displacement of up to 3.95 mm, while the ILUL station in the CW region shows a maximum displacement of 2.60 mm. The SENU station in the SW region shows a maximum displacement of 2.13 mm, the UPVK station in the NW region shows a maximum displacement of 1.95 mm, the JWLF station in the NO region shows a lower maximum displacement of 1.15 mm, and the MSVG station in the NE region shows a maximum displacement of 1.17 mm. Overall, stations in the southern SW, SE, and CW regions exhibit higher displacements compared to those in the northern NW, NE, and NO regions.

D. GNSS as a Complementary Method for Monitoring AR Events

Over the past decade, the largest melt anomalies and overall mass loss acceleration in the Greenland Ice Sheet have shifted from the southern to the northern regions [64]. Looking ahead, the mass balance of the Greenland Ice Sheet is projected to exhibit increasingly complex spatiotemporal variations. Numerous studies have indicated that future changes in Greenland's mass balance, and the consequent sea level rise contribution, will be heavily influenced by the interplay between Arctic warming, moistening, and the evolution of regional atmospheric circulation patterns [19]. ARs play a crucial role in this dynamic. The increasing frequency, expanded spatial extent, and prolonged duration of AR landfall events, along with the associated uncertainties, complicate our understanding of Greenland's mass balance dynamics. ARs not only transport warm, moisture-laden air from lower latitudes but also trigger extreme foehn-driven melt events [65]. These factors contribute to the extensive network of supraglacial streams and lakes that persist long after the summer season. Extreme melt events with compounding short- and long-term impacts reduce the ice sheet's albedo, accelerate outlet glaciers, and precondition the surface for enhanced subsequent melting. On the ocean side, AR-induced sea ice thinning or disappearance leads to the loss of buttressing and even the collapse of ice shelves at the floating glacier margins, further increasing mass loss through accelerated outlet glaciers. It is evident that future AR events will have a multifaceted and diverse impact on the ice sheet's mass balance.

It is now recognized that GNSS meteorology, in combination with other meteorological sensors, is an important tool for weather forecasting, specifically for estimating zenith water vapor content and monitoring its horizontal transport. Previous study [66] has explored the use of zenith tropospheric delay products, which are highly correlated with precipitable water vapor, from dense GNSS networks to map the movement of landfalling ARs and derive isochrones that represent the AR arrival time over a region. The GNSS-derived isochrones can track the AR arrival time at a significantly higher spatial resolution than traditional wind-profiler-based techniques, enabling the investigation of the relationship between fast AR movement and large hourly rain rates.

In addition to using GNSS to track the landfall and movement of ARs, this article further demonstrates that GNSS coordinate time series can also monitor the impacts of AR events on ice sheet dynamics. The increased precipitation and surface melting associated with AR events can have both short-term and long-term effects on ice sheet dynamics. Typically, after an AR event (e.g., 24 h later), precipitation and precipitable water vapor return to normal levels, at which point conventional monitoring methods may fail to detect the persistent impacts of the AR event. This is particularly relevant in polar regions, where precipitation from AR events can accumulate as snow or ice that persists for some time, and the warm air brought by ARs can continue to drive surface melting, with foehn effects potentially triggering melting in other parts of the Greenland Ice Sheet. In this context, GNSS networks provide a complementary technology for continuously monitoring the spatiotemporal changes in Greenland's ice sheet mass related to AR events. Our findings confirm that the mass gain (from precipitation) and mass loss (from accelerating melt and ice flow) caused by AR events have persistent and lagged characteristics. The time series of GNSS vertical displacement can effectively observe the elastic loading deformation caused by mass changes in the surrounding ice sheet. The loading approach based on multichannel SSA successfully extracted the transient signal that showed significant correlation with AR-induced precipitation. Each GNSS station can effectively monitor the elastic displacement caused by mass changes within a radius of several kilometers, and the widely distributed GNSS network across the Greenland periphery has the potential to capture the instantaneous and persistent impacts of a particular AR event on the entire Greenland Ice Sheet from different spatial perspectives.

Taken together, the use of the isochrones approach can capture the landfalling AR movement with high spatial-temporal resolution, and the use of the loading approach can monitor the overall effect of ARs on the Greenland Ice Sheet mass balance. Therefore, in addition to surface meteorological instrumentation such as wind profilers to observe vertical profiles of horizontal

winds and radio acoustic sounding systems to observe vertical profiles of potential temperature, we believe that GNSS network sensors can also provide valuable data for the spatiotemporal monitoring of AR events.

V. Disscusion

This study investigates the influence of ARs on Greenland's precipitation and crustal deformation. ARs, which transport large amounts of water vapor from lower to higher latitudes, contribute significantly to extreme weather events in polar regions. Over the past decade, ARs have made 186 landfalls in Greenland, lasting a total of 3 174 h, contributing 13.42% to the total precipitation, with greater impacts on snowfall than rainfall. This influence is more pronounced in southern Greenland, where snowfall often dominates AR events, although in warmer years, such as 2012 and 2017, rainfall contributions spiked significantly.

The spatial distribution of AR-induced precipitation highlights that the western and southern coastal regions of Greenland experience the highest rainfall and snowfall amounts. This confirms ARs' role in transporting moisture from subtropical regions to polar areas, influencing the SMB of the Greenland Ice Sheet. In contrast, AR impacts are less significant in northern Greenland, emphasizing the regional variability in their effects. In addition to precipitation, ARs contribute to measurable crustal deformation. The maximum deformation recorded was 3.86 mm, with coastal GNSS stations showing average displacements of 0.14 mm. Snowfall typically caused greater deformation than rainfall, but in some instances, extreme rainfall resulted in higher displacement. Regions closer to the coast, especially at lower latitudes, experienced more significant deformation, illustrating the link between AR precipitation and geophysical changes in Greenland.

Overall, ARs play a crucial role in Greenland's hydrology and geophysics, impacting both SMB and transient crustal deformation. These findings suggest a growing influence of ARs on extreme weather and geophysical processes in Greenland, with implications for future ice sheet stability and global climate dynamics.

VI. Conclusion

By statistically analyzing the frequency and duration of AR landfalls in Greenland, and combining this with MERRA-2 data, this study examines the distribution and magnitude of extreme precipitation caused by AR across Greenland and its basins. Based on the precipitation results, the impact of AR on crustal deformation in various regions of Greenland is analyzed. The main conclusions are as follows.

The number of AR landfalls in Greenland over ten years is 186, with a total duration of 3 174 h, accounting for 3.61% of the total time over ten years. The contribution of AR to rainfall and snowfall in Greenland is approximately 13.42%. AR's impact on rainfall typically ranges from 5% to 24%, and on snowfall from 8% to 20%. Currently, the impact of AR in most areas of southern Greenland is mainly on snowfall. Although the maximum rainfall exceeds snowfall, excluding the warm weather years of 2012 and 2017, the overall contribution rate of AR rainfall is lower than that of AR snowfall.

The contribution rate of AR-induced precipitation varies significantly across different years and regions, with some years experiencing extreme rainfall that leads to a sudden increase in the AR rainfall contribution rate. The contribution of AR to rainfall and snowfall is mostly concentrated along the western coastal region and the southern region of Greenland, with the SW region having the highest amounts of AR-induced rainfall and snowfall. This indicates that the current impact of AR varies by region and confirms that AR transports water vapor from low to high latitudes.

The maximum crustal deformation caused by AR is 3.86 mm, with the average displacement at GNSS stations peaking at 0.14 mm. The average displacement caused by AR snowfall is generally greater than that caused by AR rainfall, although the maximum displacement impact of rainfall exceeds that of snowfall. The SE region experiences the highest magnitude, while the NO region has the smallest displacement magnitude. The closer to the coastline, the closer the average and maximum displacements of a point are to their maximum values, and vice versa, they are smaller. At similar distances from the coastline, stations at lower latitudes experience greater average and maximum displacements, and vice versa. This further illustrates the significant impact of AR on snowfall displacement and the characteristics of displacement changes.

References

[1] Y. Zhu and R. E. Newell, "Atmospheric rivers and bombs," *Geophys. Res. Lett.*, vol. 21, no. 18, pp. 1999–2002, 1994.

[2] A. M. Collow et al., "An overview of ARTMIP's Tier 2 reanalysis intercomparison: Uncertainty in the detection of atmospheric rivers and their associated precipitation," *J. Geophys. Res., Atmospheres*, vol. 127, no. 8, 2022, Art. no. e2021JD036155.

[3] Q. Zhao et al., "General method of precipitable water vapor retrieval from remote sensing satellite near-infrared data," *Remote Sens. Environ.*, vol. 308, 2024, Art. no. 114180.

[4] P. Ludwig, J. G. Pinto, M. Reyers, and S. L. Gray, "The role of anomalous SST and surface fluxes over the southeastern north atlantic in the explosive development of windstorm Xynthia," *Quart. J. Roy. Meteorological Soc.*, vol. 140, no. 682, pp. 1729–1741, 2014.

[5] A. M. Ramos, R. Tomé, R. M. Trigo, M. L. Liberato, and J. G. Pinto, "Projected changes in atmospheric rivers affecting Europe in CMIP5 models," *Geophys. Res. Lett.*, vol. 43, no. 17, pp. 9315–9323, 2016.

[6] H. F. Dacre, P. A. Clark, O. Martinez-Alvarado, M. A. Stringer, and D. A. Lavers, "How do atmospheric rivers form?," *Bull. Amer. Meteorological Soc.*, vol. 96, no. 8, pp. 1243–1255, 2015.

[7] R. Lapere et al., "Polar aerosol atmospheric rivers: Detection, characteristics, and potential applications," *J. Geophys. Res., Atmospheres*, vol. 129, no. 2, 2024, Art. no. e2023JD039606.

[8] Q. Zhao, K. Liu, T. Sun, Y. Yao, and Z. Li, "A novel regional drought monitoring method using GNSS-derived ZTD and precipitation," *Remote Sens. Environ.*, vol. 297, 2023, Art. no. 113778.

[9] Q. Zhao et al., "A high-precision ZTD interpolation method considering large area and height differences," *GPS Solutions*, vol. 28, no. 1, 2024, Art. no. 4.

[10] Q. Zhao et al., "Two-step method of surface-based high-precision pet retrieval," *Atmos. Res.*, vol. 304, 2024, Art. no. 107406.

[11] P. J. Neiman, F. M. Ralph, G. A. Wick, J. D. Lundquist, and M. D. Dettinger, "Meteorological characteristics and overland precipitation impacts of atmospheric rivers affecting the west coast of North America based on eight years of SSM/I satellite observations," *J. Hydrometeorol.*, vol. 9, no. 1, pp. 22–47, 2008.

[12] P. J. Neiman et al., "The landfall and inland penetration of a flood-producing atmospheric river in Arizona. Part I: Observed synoptic-scale, orographic, and hydrometeorological characteristics," *J. Hydrometeorol.*, vol. 14, no. 2, pp. 460–484, 2013.

[13] F. M. Ralph, P. J. Neiman, and R. Rotunno, "Dropsonde observations in low-level jets over the northeastern Pacific Ocean from CALJET-1998 and PACJET-2001: Mean vertical-profile and atmospheric-river characteristics," *Monthly Weather Rev.*, vol. 133, no. 4, pp. 889–910, 2005.

[14] F. M. Ralph et al., "Atmospheric rivers emerge as a global science and applications focus," *Bull. Amer. Meteorological Soc.*, vol. 98, no. 9, pp. 1969–1973, 2017.

[15] H. Sodemann and A. Stohl, "Moisture origin and meridional transport in atmospheric rivers and their association with multiple cyclones," *Monthly Weather Rev.*, vol. 141, no. 8, pp. 2850–2868, 2013.

[16] J. J. Benedict, A. C. Clement, and B. Medeiros, "Atmospheric blocking and other large-scale precursor patterns of landfalling atmospheric rivers in the north Pacific: A CESM2 study," *J. Geophys. Res, Atmospheres*, vol. 124, no. 21, pp. 11330–11353, 2019.

[17] A. C. Martin, F. M. Ralph, A. Wilson, L. DeHaan, and B. Kawzenuk, "Rapid cyclogenesis from a mesoscale frontal wave on an atmospheric river: Impacts on forecast skill and predictability during atmospheric river landfall," *J. Hydrometeorol.*, vol. 20, no. 9, pp. 1779–1794, 2019.

[18] P. J. Neiman et al., "An airborne and ground-based study of a long-lived and intense atmospheric river with mesoscale frontal waves impacting California during CalWater-2014," *Monthly Weather Rev.*, vol. 144, no. 3, pp. 1115–1144, 2016.

[19] J. E. Box et al., "Greenland ice sheet rainfall climatology, extremes and atmospheric river rapids," *Meteorological Appl.*, vol. 30, no. 4, 2023, Art. no. e2134.

[20] L. Gimeno, I. Algarra, J. Eiras-Barca, A. M. Ramos, and R. Nieto, "Atmospheric river, a term encompassing different meteorological patterns," *Wiley Interdiscipl. Rev., Water*, vol. 8, no. 6, 2021, Art. no. e1558.

[21] J. D. Wille et al., "Intense atmospheric rivers can weaken ice shelf stability at the Antarctic Peninsula," *Commun. Earth Environ.*, vol. 3, no. 1, 2022, Art. no. 90.

[22] W. Neff, "Atmospheric rivers melt Greenland," *Nat. Climate Change*, vol. 8, no. 10, pp. 857–858, 2018.

[23] W. Li et al., "Unraveling contributions of Greenland's seasonal and transient crustal deformation during the past two decades," *Remote Sens. Environ.*, vol. 295, 2023, Art. no. 113701.

[24] M. R. Gallagher, H. Chepfer, M. D. Shupe, and R. Guzman, "Warm temperature extremes across Greenland connected to clouds," *Geophys. Res. Lett.*, vol. 47, no. 9, 2020, Art. no. e2019GL086059.

[25] J. D. Wille et al., "Antarctic atmospheric river climatology and precipitation impacts," *J. Geophys. Res., Atmospheres*, vol. 126, no. 8, 2021, Art. no. e2020JD033788.

[26] K. Mattingly, T. Mote, and X. Fettweis, "Atmospheric river impacts on Greenland ice sheet surface mass balance," *J. Geophys. Res., Atmospheres*, vol. 123, no. 16, pp. 8538–8560, 2018.

[27] J. Ran, P. Ditmar, L. Liu, Y. Xiao, R. Klees, and X. Tang, "Analysis and mitigation of biases in Greenland ice sheet mass balance trend estimates from grace mascon products," *J. Geophys. Res., Solid Earth*, vol. 126, no. 7, 2021, Art. no. e2020JB020880.

[28] T. Zhao et al., "Artificial intelligence for geoscience: Progress, challenges and perspectives," *Innovation*, vol. 5, no. 5, Sep. 2024, doi: 10.1016/j.xinn.2024.100691.

[29] W. Li et al., "Contributions of Greenland GPS observed deformation from multisource mass loading induced seasonal and transient signals," *Geophysical Res. Lett.*, vol. 47, no. 15, 2020, Art. no. e2020GL088627.

[30] B. Zhang, L. Liu, S. A. Khan, T. v. Dam, E. Zhang, and Y. Yao, "Transient variations in glacial mass near Upernavik Isstrøm (West Greenland) detected by the combined use of GPS and grace data," *J. Geophys. Res., Solid Earth*, vol. 122, no. 12, pp. 10–626, 2017.

[31] K. S. Mattingly et al., "Strong summer atmospheric rivers trigger Greenland Ice Sheet melt through spatially varying surface energy balance and cloud regimes," *J. Climate*, vol. 33, no. 16, pp. 6809–6832, 2020.

[32] S. Adusumilli, M. A. Fish, H. A. Fricker, and B. Medley, "Atmospheric river precipitation contributed to rapid increases in surface height of the west Antarctic ice sheet in 2019," *Geophys. Res. Lett.*, vol. 48, no. 5, 2021, Art. no. e2020GL091076.

[33] J. E. Box, D. H. Bromwich, and L.-S. Bai, "Greenland ice sheet surface mass balance 1991–2000: Application of polar MM5 mesoscale model and in situ data," *J. Geophys. Res., Atmospheres*, vol. 109, no. D16, Aug. 2004, Art. no. 2003JD004451, doi: 10.1029/2003JD004451.

[34] K. C. Schuenemann and J. J. Cassano, "Changes in synoptic weather patterns and Greenland precipitation in the 20th and 21st centuries: 1. Evaluation of late 20th century simulations from IPCC models," *J. Geophys. Res.: Atmospheres*, vol. 114, no. D20, 2009, doi: 10.1029/2009JD011705.

[35] K. C. Schuenemann and J. J. Cassano, "Changes in synoptic weather patterns and Greenland precipitation in the 20th and 21st centuries: 2. Analysis of 21st century atmospheric changes using self-organizing maps," *J. Geophys. Res., Atmospheres*, vol. 115, no. D5, Mar. 2010, Art. no. 2009JD011706, doi: 10.1029/2009JD011706.

[36] M. R. V. d. Broeke et al., "On the recent contribution of the Greenland ice sheet to sea level change," *Cryosphere*, vol. 10, no. 5, pp. 1933–1946, 2016.

[37] J. D. Wille et al., "West antarctic surface melt triggered by atmospheric rivers," *Nature Geosci.*, vol. 12, no. 11, pp. 911–916, 2019.

[38] B. Zhang and Y. Yao, "Precipitable water vapor fusion based on a generalized regression neural network," *J. Geodesy*, vol. 95, no. 3, 2021, Art. no. 36.

[39] B. Zhang et al., "Geodetic and model data reveal different spatio-temporal patterns of transient mass changes over Greenland from 2007 to 2017," *Earth Planet. Sci. Lett.*, vol. 515, pp. 154–163, 2019.

[40] B. Zhang et al., "Geodetic measurements reveal short-term changes of glacial mass near Jakobshavn Isbræ (Greenland) from 2007 to 2017," *Earth Planet. Sci. Lett.*, vol. 503, pp. 216–226, 2018.

[41] R. S. Fausto, D. V. As, J. E. Box, W. Colgan, and P. L. Langen, "Quantifying the surface energy fluxes in south Greenland during the 2012 high melt episodes using in-situ observations," *Front. Earth Sci.*, vol. 4, 2016, Art. no. 82.

[42] R. S. Fausto, D. v. As, J. E. Box, W. Colgan, P. L. Langen, and R. H. Mottram, "The implication of nonradiative energy fluxes dominating Greenland ice sheet exceptional ablation area surface melt in 2012," *Geophys. Res. Lett.*, vol. 43, no. 6, pp. 2649–2658, 2016.

[43] W. Neff, G. P. Compo, F. M. Ralph, and M. D. Shupe, "Continental heat anomalies and the extreme melting of the Greenland ice surface in 2012 and 1889," *J. Geophys. Res., Atmospheres*, vol. 119, no. 11, pp. 6520–6536, 2014.

[44] J. F. Danco, A. M. DeAngelis, B. K. Raney, and A. J. Broccoli, "Effects of a warming climate on daily snowfall events in the northern hemisphere," *J. Climate*, vol. 29, no. 17, pp. 6295–6318, 2016.

[45] S. H. Doyle et al., "Amplified melt and flow of the Greenland ice sheet driven by late-summer cyclonic rainfall," *Nat. Geosci.*, vol. 8, no. 8, pp. 647–653, 2015.

[46] M. R. Gallagher, M. D. Shupe, H. Chepfer, and T. L'Ecuyer, "Relating snowfall observations to Greenland ice sheet mass changes: An atmospheric circulation perspective," *Cryosphere*, vol. 16, no. 2, pp. 435–450, 2022.

[47] K. S. Mattingly, C. A. Ramseyer, J. J. Rosen, T. L. Mote, and R. Muthyala, "Increasing water vapor transport to the Greenland ice sheet revealed using self-organizing maps," *Geophys. Res. Lett.*, vol. 43, no. 17, pp. 9250–9258, 2016.

[48] B. Noël et al., "Evaluation of the updated regional climate model RACMO2. 3: Summer snowfall impact on the Greenland ice sheet," *Cryosphere*, vol. 9, no. 5, pp. 1831–1844, 2015.

[49] I. V. Gorodetskaya, M. Tsukernik, K. Claes, M. F. Ralph, W. D. Neff, and N. P. V. Lipzig, "The role of atmospheric rivers in anomalous snow accumulation in East Antarctica," *Geophys. Res. Lett.*, vol. 41, no. 17, pp. 6199–6206, 2014.

[50] J. T. Lenaerts, B. Medley, M. R. v. d. Broeke, and B. Wouters, "Observing and modeling ice sheet surface mass balance," *Rev. Geophys.*, vol. 57, no. 2, pp. 376–420, 2019.

[51] J. Li, W. Li, C. Shum, F. Li, S. Zhang, and J. Lei, "Unraveling the contributions of atmospheric rivers on Antarctica crustal deformation and its spatiotemporal distribution during the past decade," *Geophys. J. Int.*, vol. 235, no. 2, pp. 1325–1338, 2023.

[52] M. L. Maclennan et al., "Climatology and surface impacts of atmospheric rivers on West Antarctica," *Cryosphere*, vol. 17, no. 2, pp. 865–881, 2023.

[53] M. L. Maclennan and J. T. Lenaerts, "Large-scale atmospheric drivers of snowfall over Thwaites Glacier, Antarctica," *Geophys. Res. Lett.*, vol. 48, no. 17, 2021, Art. no. e2021GL093644.

[54] Z. Li, B. F. Chao, Z. Zhang, L. Jiang, and H. Wang, "Greenland interannual ice mass variations detected by grace time-variable gravity," *Geophys. Res. Lett.*, vol. 49, no. 19, 2022, Art. no. e2022GL100551.

[55] Z. Li, B. F. Chao, H. Wang, and Z. Zhang, "Antarctica ice-mass variations on interannual timescale: Coastal dipole and propagating transports," *Earth Planet. Sci. Lett.*, vol. 595, 2022, Art. no. 117789.

[56] E. Rignot, I. Velicogna, M. R. van den Broeke, A. Monaghan, and J. T. M. Lenaerts, "Acceleration of the contribution of the Greenland and Antarctic ice sheets to sea level rise," *Geophys. Res. Letters*, vol. 38, no. 5, 2011, doi: 10.1029/2011GL046583.

[57] G. Blewitt, W. Hammond, and C. Kreemer, "Harnessing the GPS data explosion for interdisciplinary science," *Eos*, vol. 99, no. 2, 2018, Art. no. e2020943118.
[58] H. J. Zwally, M. B. Giovinetto, M. A. Beckley, and J. L. Saba, "Antarctic and Greenland drainage systems," GSFC Cryospheric Sci. Lab., Tech. Rep. 265, 2012.
[59] M. L. Maclennan, J. T. Lenaerts, C. Shields, and J. D. Wille, "Contribution of atmospheric rivers to antarctic precipitation," *Geophys. Res. Lett.*, vol. 49, no. 18, 2022, Art. no. e2022GL100585.
[60] H. R. Martens, L. Rivera, and M. Simons, "LoadDef: A Python-based toolkit to model elastic deformation caused by surface mass loading on spherically symmetric bodies," *Earth Space Sci.*, vol. 6, no. 2, pp. 311–323, 2019.
[61] Q. Kong, L. Zhang, J. Han, C. Li, W. Fang, and T. Wang, "Analysis of coordinate time series of DORIS stations on Eurasian plate and the plate motion based on SSA and FFT," *Geodesy Geodynamics*, vol. 14, no. 1, pp. 90–97, 2023.
[62] B. Zhang, L. Liu, Y. Yao, T. v. Dam, and S. A. Khan, "Improving the estimate of the secular variation of Greenland ice mass in the recent decades by incorporating a stochastic process," *Earth Planet. Sci. Lett.*, vol. 549, 2020, Art. no. 116518.
[63] T. Zhang, W.-B. Shen, W. Wu, B. Zhang, and Y. Pan, "Recent surface deformation in the Tianjin area revealed by Sentinel-1A data," *Remote Sens.*, vol. 11, no. 2, 2019, Art. no. 130.
[64] J. Mouginot et al., "Forty-six years of Greenland ice sheet mass balance from 1972 to 2018," *Proc. Nat. Acad. Sci.*, vol. 116, no. 19, pp. 9239–9244, 2019.
[65] K. S. Mattingly et al., "Increasing extreme melt in northeast Greenland linked to foehn winds and atmospheric rivers," *Nature Commun.*, vol. 14, no. 1, 2023, Art. no. 1743.
[66] M. Wang, J. Wang, Y. Bock, H. Liang, D. Dong, and P. Fang, "Dynamic mapping of the movement of landfalling atmospheric rivers over southern California with GPS data," *Geophys. Res. Lett.*, vol. 46, no. 6, pp. 3551–3559, 2019.

Wenhao Li received the B.S. degree from Liaoning Technical University, Fuxin, China, in 2014, and the Ph.D. degree in geodesy and survey engineering from Wuhan University, Wuhan, China, in 2020.

He is currently working with the School of Geomatics Science and Technology, Nanjing Tech University, Nanjing, China, and the State Key Laboratory of Cieo-information Engineering, Xi'an, China. His research interests include geodetic data processing theory, global positioning system time-series analysis, and mass balance of polar ice caps.

Xinyu Qin received the B. E. degree in surveying and mapping engineering in 2022 from the College of Geomatics Science and Technology, Nanjing Tech University, Nanjing, China, where he is currently working toward the M.S. degree in geography.

His research interests include global positioning system time-series analysis and mass balance of polar ice caps.

Tingting Zhu received the B.S. degree in surveying and mapping from Nanjing Normal University, Nanjing, China, in 2012, and the M.S. and Ph.D. degrees in Geodesy and Geomatics from the State Key Laboratory of Information Engineering in Surveying, Mapping, and Remote Sensing (LIESMARS), Wuhan University, Wuhan, China, in 2014 and 2017.

She is currently working with the College of Geomatics Science and Technology, Nanjing Tech University, Nanjing. Her research interests include change detection from high-resolution remotely sensed imagery and multisensor remote sensing in the cryosphere.

Jintao Lei received the Ph.D. degree in geodesy and surveying engineering from the Chinese Antarctic Center of Surveying and Mapping, Wuhan University, Wuhan, China, in 2018.

He was a Postdoctoral Fellow with the Department of Land Surveying and Geo-Informatics, Hong Kong Polytechnic University, until 2022. He is currently an Assistant Professor with the School of Civil Engineering and Architecture, Guangxi University, Nanning, China. His main research interests include multiglobal navigation satellite system positioning, time-series analysis, and structural health monitoring in civil engineering.

C. K. Shum received the Ph.D. degree from the University of Texas at Austin, Austin, TX, USA, in 1982 .

He is currently a Professor and Distinguished University Scholar with the Division of Geodetic Science, School of Earth Sciences, The Ohio State University, Columbus, OH, USA. His research interests include sea-level and climate science on the observation and quantification of geophysical processes contributing to present-day sea-level change.

Dr. Shum is a Fellow of the American Association for the Advancement of Science, and a Fellow of the International Association of Geodesy.

Fei Li received the B.S. degree from the University of Science and Technology of China, Hefei, China, in 1982, and the Ph.D. degree from the Institute of Geodesy and Geophysics of Chinese Sciences Academy, Wuhan, China, in 1992 .

He is currently the Director of the Chinese Antarctic Research Center of Surveying and Mapping, Wuhan University. He is also the vice-President of Wuhan University, Wuhan, China. His research interests include the polar remote sensing, Geodesy and geophysics in polar research, Geophysical inversion in Lunar gravity and internal structure.

Shengkai Zhang received the B.S. degree from the Wuhan Technical University of Surveying and Mapping, Wuhan, China, in 1998, and the Ph.D. degree in geodesy from Wuhan University, Wuhan, in 2006. He worked in Chinese Antarctic Center of Surveying and Mapping, Wuhan University

He is an Associate Professor with Chinese Antarctic Center of Surveying and Mapping, Wuhan University. His research interests include polar geophysics and geodesy.